JGR Oceans

RESEARCH ARTICLE
10.1029/2020JC016700

Key Points:

- Persistent seasonal eutrophication/hypoxia exhibits remarkable spatiotemporal variability in the coastal transition zone off the Pearl River Estuary
- Variable wind forcing regulates three-dimensional transport and characterizes the spatiotemporal variability of the hypoxia
- Variable wind-driven circulation regulates hypoxia variability by altering the nutrient-rich river plume's path, the strength of the mixing, and water residence time

Correspondence to:
J. Gan,
magan@ust.hk

Citation:
Li, D., Gan, J., Hui, C., Yu, L., Liu, Z., Lu, Z., et al. (2021). Spatiotemporal development and dissipation of hypoxia induced by variable wind-driven shelf circulation off the Pearl River Estuary: Observational and modeling studies. *Journal of Geophysical Research: Oceans*, *126*, e2020JC016700. https://doi.org/10.1029/2020JC016700

Received 9 AUG 2020
Accepted 27 DEC 2020

Spatiotemporal Development and Dissipation of Hypoxia Induced by Variable Wind-Driven Shelf Circulation off the Pearl River Estuary: Observational and Modeling Studies

Dou Li[1], Jianping Gan[1], Chiwing Hui[1], Liuqian Yu[1], Zhiqiang Liu[1,2], Zhongming Lu[1], Shuh-ji Kao[3], and Minhan Dai[3]

[1]Department of Ocean Science, Department of Mathematics and Center for Ocean Research in Hong Kong and Macau, Hong Kong University of Science and Technology, Hong Kong, China, [2]Department of Ocean Science and Engineering, Southern University of Science and Technology, Shenzhen, China, [3]State Key Lab of Marine Environmental Science, Xiamen University, Xiamen, China

Abstract Observations reveal the high spatiotemporal variability of the hypoxia in the western and eastern coastal transition zones (WCTZ and ECTZ) off the Pearl River Estuary (PRE). We utilized data from cruise observations, buoy mooring, and a three-dimensional model based on ROMS to investigate the hypoxia variability response to the typical synoptic variation of the summer monsoon, i.e., from prevailing upwelling-favorable wind (UFW), the ensuing episodic upwelling relaxation (URW), downwelling (DFW), to downwelling relaxation wind (DRW). During the UFW, we found that the northeastward shelf current converges with nutrient-rich river plume, forms strong stratification, and provides hubs for depositing detritus for hypoxia to develop in the CTZ. The ensuing URW and DFW forcing alters the transport to advect the plume and detritus westward, weakens vertical mixing, and enhances hypoxia in the WCTZ. Correspondingly, opposite conditions occur in the ECTZ as the plume veers westward during the URW and DFW. Contrarily, the weakening westward transport during the DRW forcing restores the biophysical conditions to their states when there is an UFW event. We found that varying wind-driven circulation interacts with the plume to jointly regulate the transport of nutrient and detritus, water vertical mixing, and residence time, and, thus, the hypoxia variability in the CTZ. The variability of hypoxia in the CTZ is less controlled by the river discharges once biogeochemical conditions become saturated. Our study illustrates the biophysical control of hypoxia variability that is frequently observed in estuaries and coastal oceans.

Plain Language Summary Spatiotemporal hypoxia variability was observed in the western and eastern coastal transition zones (CTZ) off the Pearl River Estuary by cruises and a moored buoy. The biophysical responses to the typical summer monsoon synoptic variation in the prevailing southwesterly upwelling-favorable wind, the ensuing episodic upwelling relaxation, downwelling, to downwelling relaxation wind were investigated by observed data and by a three-dimensional modeling study. We found that varying wind-driven circulation interacting with river plume jointly regulate the transport of nutrient and detritus, water vertical mixing and residence time, the hypoxia variability in the CTZ. Our study illustrates the biophysical control of hypoxia variability that is frequently observed in the global coastal oceans.

1. Introduction

Estuaries and coastal waters worldwide are increasingly threatened by hypoxia (dissolved oxygen, DO, <2 mg L^{-1}) (Breitburg et al., 2018; Diaz & Rosenberg, 2008; Fennel & Testa, 2019). Hypoxia is modulated by both variable physical processes (e.g., Hetland & DiMarco, 2008; Zhang et al., 2018) and biological responses (e.g., Carstensen et al., 2014) over different time scales. While general hypoxia formation and distribution have been widely reported, the variability of hypoxia response to the highly variable oceanic biophysical conditions has not been sufficiently discussed.

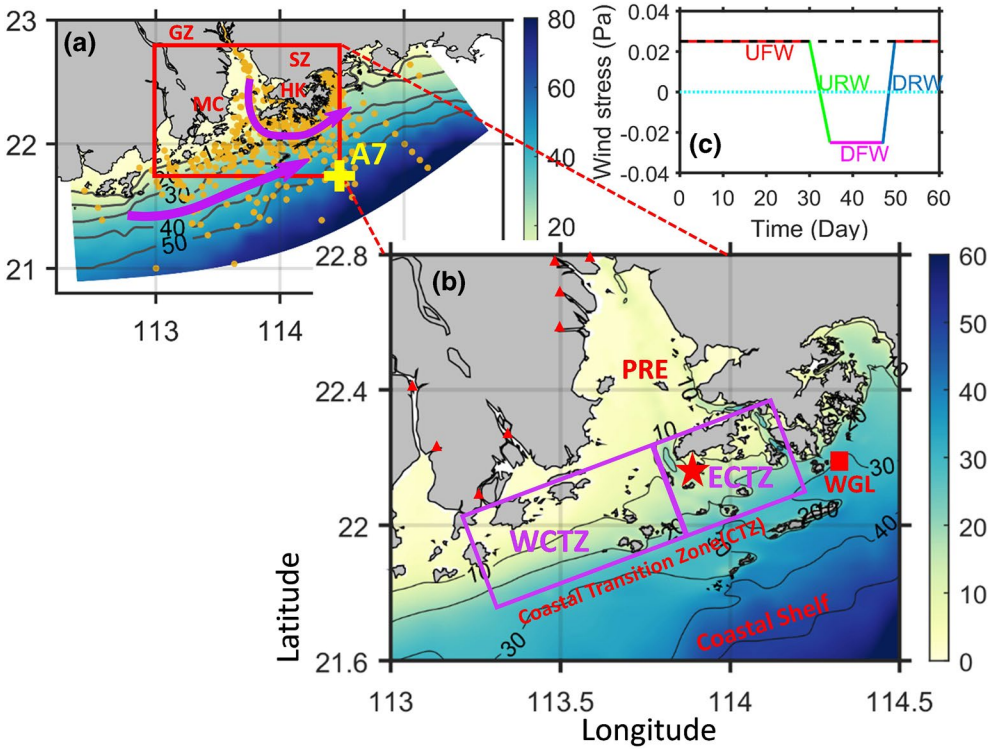

Figure 1. Map of (a) model domain with topography and isobaths (in meters) and (b) the enlarged area of the Pearl River Estuary (PRE) and adjacent shelf off Hong Kong, (c) time series of typical upwelling-favorable wind (UFW) used in the Case W1 (black dashed line) and synoptic variation of summer monsoon used in Case W2 (colored line), in which wind transited from UFW, upwelling relaxation wind (URD), downwelling favorable wind (DFW), to downwelling relaxation wind (DRW). The magenta arrows in (a) show the general upwelling-favorable-wind-driven circulation during summer. GZ = Guangzhou; SZ = Shenzhen; MC = Macao; HK = Hong Kong. The yellow cross shows the location of Station A7. The orange dots represent the sampling locations of all cruises listed in Table 1. WCTZ and ECTZ in (b) are the western and eastern coastal transition zones (CTZ). Red triangles are the locations of river outlets. The red star and square show the location of the buoy mooring and Waglan Island (WGL), respectively. The dashed cyan line in (c) shows the value of alongshore wind stress = 0.

The Pearl River Estuary (PRE) is embedded into the northern South China Sea (SCS). The estuary is a link between the Pearl River with an annual mean discharge of ~10,000 m^3 s^{-1} and adjacent continental shelf (Figure 1). During summer, hypoxia frequently occurs in the coastal transition zone (CTZ) bordering PRE and the adjacent shelf (Figure 1b), where the convergence induced by local hydrodynamics and nutrient from the river plume provides a biophysical hub favoring detritus accumulation and oxygen depletion (Li et al., 2020). The biogeochemical mechanisms controlling the hypoxia formation in the CTZ have been investigated using observations and numerical simulations. For example, eutrophication is the most plausible driver of oxygen deficiency in CTZ (Qian et al., 2018). The autochthonous organic matter fueled by nutrient enrichment is the primary oxygen-consuming source (Su et al., 2017). Besides, sediment oxygen consumption is the main contributor to the bottom oxygen depletion (Lu et al., 2018; Wang et al., 2017; Zhang & Li, 2010) mainly because of the shallow topography and high deposition flux of organic matter in the hypoxic region (Yu et al., 2020; Zhang et al., 2009).

Previous studies often treated hypoxia as a quasi-steady phenomenon due to a poor understanding of the underlying oceanic variability. Gan et al. (2014) investigated the ecosystem responses to P limitation in the plume, and Lu et al. (2018) studied the formation of hypoxia in the western part of PRE under steady forcings of nutrient load from river discharge and upwelling-favorable wind condition. However, the hypoxia in the CTZ is spatiotemporally variable as reported by Harrison et al. (2008) and Cui et al. (2019). We confirmed this variability by the field surveys presented in this paper. The spatiotemporal variability of the biogeochemical processes and hypoxia in the PRE are controlled by multiple biophysical external stressors

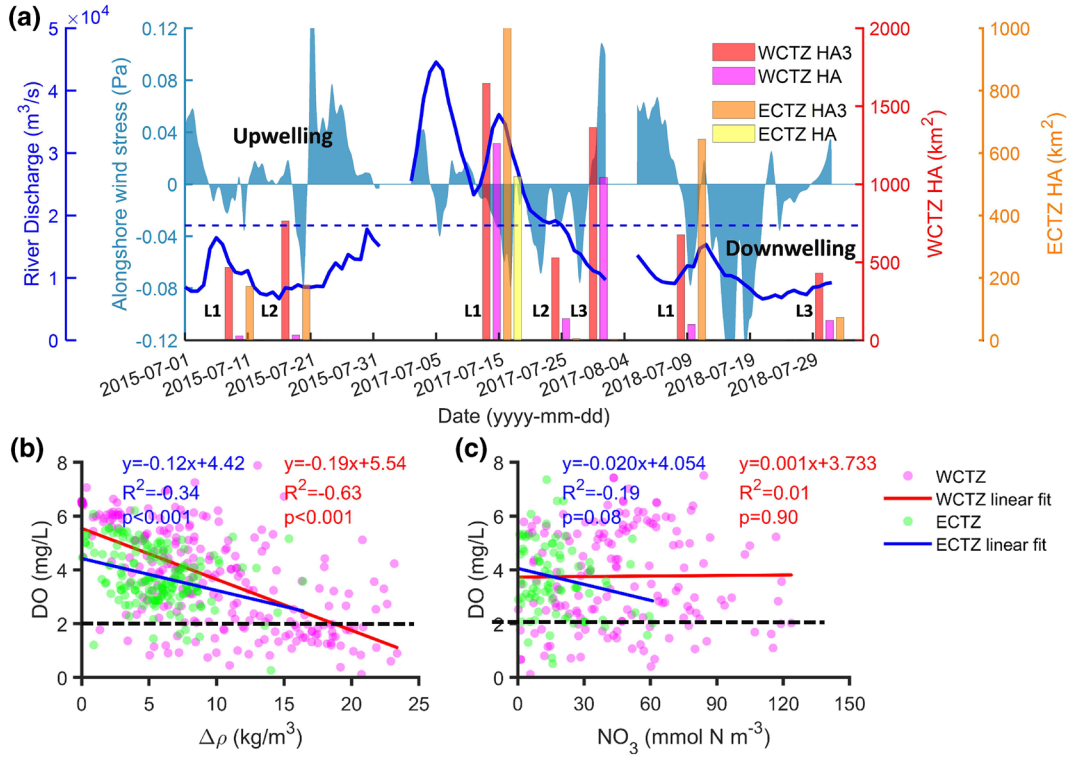

Figure 2. (a) Time series of alongshore wind stress (light blue area, positive/negative values directed northeastward/southwestward, respectively), river discharge (dark blue line), and the WCTZ and ECTZ hypoxia areas under the limit of DO < 3 mg L^{-1} (HA3) and DO < 2 mg L^{-1} (HA) of different cruises during the summers of 2015, 2017, and 2018. The blue dashed line depicts the multiyear averaged river discharge of 18,400 m^3 s^{-1}. Distributions of bottom DO as a function of (b) surface-bottom density difference ($\Delta\rho$) and (c) surface NO_3 within the WCTZ (magenta dots) and ECTZ (green dots) based on the cruise observations. The red and blue solid lines represent the linear fit of DO and $\Delta\rho$ and NO_3 with R^2 and P representing the correlation coefficients and P-values in the WCTZ and ECTZ, respectively. The black dashed lines depict DO = 2 mg L^{-1}. WCTZ, western coastal transition zones; ECTZ, eastern coastal transition zones.

such as nutrient loads and river discharge (Lu et al., 2018; Qian et al., 2018), wind speed and direction (Wei et al., 2016), tides, and coastal currents (Li et al., 2020).

The wind-driven coastal circulation transports and distributes the nutrient-rich river plume in the CTZ (Gan et al., 2009a; Liu & Gan, 2020). During summer, although dominated by the prevailing southwesterly monsoon, the wind varies roughly within a synoptic time scale and experiences upwelling-favorable wind (UFW, southwesterly or northeastward), upwelling relaxation wind (URW, i.e., the period during which wind shifts from UFW to downwelling favorable wind), episodic downwelling favorable wind (DFW, northeasterly or southwestward), and downwelling relaxation wind (DRW, Figures 2 and 3). As a consequence, the wind-driven circulations vary a great deal in the CTZ, and the circulations vary with plume conditions (Gan et al., 2009b; Ou et al., 2009; Zu & Gan, 2015; Zu et al., 2014).

The varying wind-driven circulation alters the nutrient and organic matter distribution and other biophysical conditions that determine the location and magnitude of hypoxia in the CTZ, as shown in our field surveys and previous studies (Wei et al., 2016; Yin et al., 2004; Zhao et al., 2020). As compared with the conditions under UFW that tend to upwell nutrient-rich deep water to the upper layer, DFW appears to be unfavorable for hypoxia in the Gulf of Mexico, Oregon coast, and Changjiang Estuary (Adams et al., 2013; Feng et al., 2014; Siedlecki et al., 2015; Zhang et al., 2018). The main reasons for the weakened hypoxia were the prolonged DFW forcing that led to the shoreward Ekman confinement of the nutrient-rich water, weakened/shutdown upslope nutrient transport, and enhanced nearshore mixing. These indicate the importance of the coastal circulation in determining the nutrient transport/distribution, nutrient source/sink, and water column stability for eutrophication and hypoxia. However, the effect of the wind-driven coastal

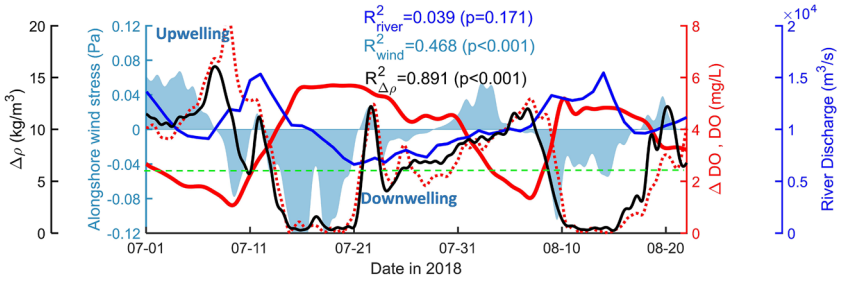

Figure 3. Time series of wind stress at the WGL (light blue shaded curve), river discharge (blue line), surface-bottom density difference ($\Delta\rho$, black line), bottom DO (red solid line), and surface-bottom DO difference (ΔDO,red dashed line) from July 1 to August 21 in 2018 measured by the moored buoy. The green dashed line indicates DO = 2 mg L^{-1}. R^2_{river}, R^2_{wind}, and $R^2_{\Delta\rho}$ are the correlation coefficients for bottom DO and river discharge, wind, and $\Delta\rho$ with *P*-values in parentheses, respectively.

circulation on hypoxia may vary and is subject to the topography, wind stress pattern and intensity, characteristics of river discharge, and other local biophysical conditions. This study investigates the responses of the variable biophysical processes, such as the circulation and the associated stratification, mixing, residence time, transport in nutrient and organic matter, and eutrophication/hypoxia variability, to the typical synoptic wind transition among prevailing UFW, URW, DFW, and DRW that have frequently been observed in the PRE (Gan et al., 2015) and in other coastal regions (e.g., west coast of US (Gan & Allen, 2002; Spitz et al., 2005)) during the prevailing upwelling season.

Besides, the biogeochemical responses to varying wind and river discharge are nonlinear. They involve feedbacks that might amplify or dampen the physical responses, and their responses are not fully explored in the PRE on a synoptic-scale.

Advancing our understanding of the spatiotemporal variability of hypoxia in a synoptic-scale and quantification of the variability paints a clearer picture for biophysical processes to better interpret the observed phenomena that are often spatiotemporally limited. This paper aims to investigate how the observed spatiotemporally variable eutrophication and hypoxia in the CTZ off the PRE respond to variable biophysical stressors by combining summer cruises surveys, buoy time series data, and a process-oriented modeling investigation. Following the introduction, we presented the observed data and the numerical model in Section 2. The observational and modeling results during the UFW, URW, DFW, and DRW were analyzed in Section 3. In Section 4, we quantified and discussed the impacts of the varying wind-driven shelf circulation and river discharge on hypoxia. Finally, we summarized our results and their applicability to other estuarine systems in Section 5.

2. Observations and Ocean Model

2.1. Observations

Eight field surveys were conducted to examine the spatiotemporal variability of biophysical parameters in the PRE and adjacent shelf in July of 2015, 2017, and 2018 (Table 1). In total 552 vertical profiles of salinity, temperature, DO, and chlorophyll were measured with a calibrated Sea-Bird SBE17plus. DO and chlorophyll from sensors were calibrated by the onboard DO measured by the spectrophotometric Winkler method and chlorophyll measured by the standard fluorometric method (Parsons, 2013). We run nutrient samples on a Technicon AA3 Auto-Analyzer and analyzed nitrate with the copper-cadmium column reduction method (Han et al., 2012) with a detection limit of 0.1 μmol L^{-1}.

In addition to cruise measurements, we deployed a real-time marine monitoring buoy system south of Hong Kong at a water depth of 12 m (22.153°N, 113.900°E, Figure 1b). The buoy measured temperature, salinity, and DO by HydroCAT-EP every 15 min at the surface and bottom layers. The instruments equipped in the buoy, including CTD and DO sensor, were calibrated before deployment. The water column stability was represented by the surface and bottom difference. Daily-smoothed buoy data from July 1 to August 21 in 2018 was used to examine the response of water column stability and bottom DO to the varying wind and

Table 1
List of Observation Time, Averaged River Discharge Rates, and Wind Stress for 8 Summer Cruises During 2015, 2017, and 2018

Cruise number	Year	Leg symbol	Number of profiles	Period	Alongshore wind stress (Pa)	Cross-shore wind stress (Pa)	River discharge rate (m^3/s)
1	2015	L1	100	Jul 6–Jul 15	−0.002	−0.005	10,812
2	2015	L2	106	Jul 15–Jul 24	0.024	0.029	8,515
3	2017	L1	84	Jul 11–Jul 22	−0.027	−0.007	28,328
4	2017	L2	47	Jul 22–Jul 28	−0.029	−0.017	17,250
5	2017	L3	54	Jul 28–Jul 30	0.003	−0.003	12,389
6	2018	L1	66	Jul 6–Jul 14	−0.028	−0.012	12,012
7	2018	L2	57	Jul 20–Jul 25	−0.013	0.007	7,074
8	2018	L3	38	Jul 28–Jul 31	0.011	0.013	8,369

river discharge. The discharge rate of Pearl River was obtained from different hydrological stations covering the entire river streams from the Information Center of Water Resources (Bureau of Hydrology, the Ministry of Water Resources of PR China). Wind data at Waglan Island (WGL; Figure 1b) was obtained from the Hong Kong Observatory (https://www.hko.gov.hk/tc/cis/form/online_reqform.htm#).

2.2. Coupled Physical-Biogeochemical Model

A coupled physical-biogeochemical model based on the Regional Ocean Modeling System (ROMS) (Shchepetkin & McWilliams, 2005) was used in this study, in which a biological module consisting of nitrogen, phosphorus, phytoplankton, zooplankton, detritus, and oxygen (Gan et al., 2014) adapted from Fennel et al. (2006) was configured. The model domain covered the PRE and the adjacent shelf (Figure 1a) and had 400 × 441 horizontal orthogonal curvilinear cells and 30 terrain-following vertical layers on S-coordinate, with a horizontally higher resolution near coastal region (<100 m), lower resolution (~1 km) near the southern boundary and vertically refined at the surface and bottom layers. The model used a level-2.5 turbulent closure scheme for vertical mixing provided by Mellor and Yamada (1982), a third-order upwind-biased scheme for horizontal momentum advection, and a multidimensional positive definite advection transport algorithm (MPDATA) to approximate the advection terms of tracers (Smolarkiewicz & Margolin, 1998). In the biological model, the oxygen equation was expressed as

$$\text{Rate} = \text{HADV} + \text{VADV} + \text{HDIF} + \text{VDIF} + \text{Phot} + \text{Nitrif} + \text{Remin} + \text{Metab} + \text{Rea} + \text{SOD} \quad (1)$$

Terms on the right-hand side represent the processes of horizontal advection (HADV), vertical advection (VADV), horizontal diffusion (HDIF), vertical diffusion (VDIF), photosynthesis (Phot), nitrification (Nitri), metabolism (Metab) of zooplankton, remineralization (Remin) of small detritus and large detritus, reaeration (Rea) or air-sea exchange at surface, and sediment oxygen demand (SOD) due to the remineralization of detritus and sinking phytoplankton at the bottom, respectively. We set the biological parameters adopted in the NPPZD-oxygen model in the PRE based on previous studies in this region (Table A1 in Appendix) (Gan et al., 2014; Lu et al., 2018).

Aimed to identify the processes governing the spatiotemporal variability of eutrophication and hypoxia, the process-oriented model was initialized from rest with a horizontally uniform temperature, salinity, nitrate (NO_3), phosphate (PO_4), DO, chlorophyll, and other biogeochemical profiles obtained at Station A7 (Figure 1a) as in Gan et al. (2014). We imposed tidal forcing extracted from the Oregon State University Tidal Inversion Software (OTIS) (Egbert & Erofeeva, 2002) at the open boundaries (OBs). A tidal-subtidal open boundary condition (TST-OBC) (Liu & Gan, 2016) that integrates the active OBC of Gan and Allen (2005) with Flather-type OBC and accommodates the concurrent tidal and subtidal forcing was applied to both barotropic and baroclinic variables along the open boundary. The daily-average solar radiation was set to 195 W m^{-2} with a diurnal cycle distribution. We set salinity, temperature, NO_3, PO_4, and DO of the river

discharge to 3 PSU, 28.6 °C, 90 mmol m^{-3}, 1.5 mmol m^{-3}, and 3 mg L^{-1}, respectively (Cai et al., 2004). More detailed model implementations are described in Lu et al. (2018) and Li et al. (2020).

To better identify the fundamental physical-biogeochemical responses to essential forcing of winds and river discharge, we conducted process-oriented modeling studies using simplified but representative forcing that mimics the observed characteristics. We used a multiyear summer averaged river discharge rate, 18,400 m^3 s^{-1}, as the base river discharge in Case W1. The multiyear averaged summer wind stress (i.e., UFW, 0.025 Pa, and directed 23° anticlockwise from real east) was used to run for 55 days in the Case W1 (Figure 1c). The model was spun-up in ~20 days and reached a quasi-steady state of upwelling. In Case W2 shown in Figure 1c, we applied spatially uniform UFW before Day 30. The wind forcing was then linearly shifted to the URW from Day 31 to Day 35, and subsequently to DFW (−0.025 Pa, directed 23° anticlockwise from real west) from Day 36 to Day 47. DRW (i.e., linearly increasing from −0.025 to 0.025 Pa) was applied from Day 48 to Day 50, followed by UFW from Day 50 to Day 55. The daily-averaged outputs from simulations were used in this paper. The biophysical and hypoxia features of the model result were validated by cruise data in Li et al. (2020), which established a level of confidence for us to investigate the underlying coupled physical-biogeochemical dynamics of the hypoxia variability.

3. Results

3.1. Observed Results

3.1.1. Temporal Variation of Hypoxia

Time series of the alongshore wind stress, river discharge, and hypoxic area within the western and eastern coastal transition zones (WCTZ and ECTZ) of all cruises are shown in Figure 2a. The total hypoxic area (sum of WCTZ and ECTZ), defined as DO < 2 mg L^{-1}, varied remarkably from ~28 km^2 in 2015 L1 to ~1,790 km^2 in 2017 L1. To avoid the approximation errors and information loss caused by the low observational resolution and relatively weak hypoxia during the survey period, we also calculated the area of water with DO < 3 mg L^{-1} (referred to as HA3). The results indicate a high temporal hypoxia variability in the CTZ. Seven episodes of hypoxia or near hypoxia, defined as DO < 3 mg L^{-1}, occurred in the WCTZ among eight cruises except for 2018 L2 when a typhoon occurred in the northern South China Sea. Only five episodes of hypoxia were observed in the ECTZ. The first feature is that both HA and HA3 are larger during the period of high river discharge. With higher river discharge during 2017 L1, about 1.5 times of the multiyear average discharge (18,400 m^3 s^{-1}), HA3 was about 4.4 times larger than that in 2015 L1 and 2.2 times larger than that in 2018 L1 in the CTZ. Another prominent feature is that HA3 in the ECTZ is generally smaller and more sensitive to wind variation than that in the WCTZ. When the wind transited from UFW to DFW during L1 and L2 in 2017, HA3 decreased by 68% and 99% in the WCTZ and ECTZ, respectively.

Based on the statistical analysis of the cruise observations, we find a close relationship between bottom DO and vertical stratification ($\Delta\rho$) under different forcing conditions, which is markedly affected by the extension of the river plume over the CTZ (Figure 2b). Bottom DO decreases significantly ($P < 0.001$) with increasing $\Delta\rho$ in the CTZ, indicating the vital role of stratification in the formation of hypoxia. Besides, hypoxia occurs more frequently the upstream of the plume's path within the WCTZ, where stratification is more robust, and the correlation between bottom DO and $\Delta\rho$ ($R^2 = -0.63$) is higher than in the ECTZ (−0.34). However, no significant correlation ($P > 0.001$) is found between DO and surface NO_3 in the CTZ (Figure 2c), especially within the WCTZ. Although not significant, the bottom DO negatively correlates with surface NO_3 ($R^2 = -0.19$) in the ECTZ.

The time series data at the buoy moored near the ECTZ (Figure 1b) from July 1 to August 21 in 2018 show the temporal correlation between bottom DO and different stressors. Figure 3 presents the time series of the daily-averaged bottom DO, surface and bottom difference of density ($\Delta\rho$) and DO (ΔDO), and simultaneous alongshore wind stress at the WGL and river discharge. The wind experienced two cycles of UFW, URW, DFW, and DRW.

The most prominent feature is that $\Delta\rho$, regulated by the wind and river discharge, and ΔDO varies synchronously at the same phase ($R^2 = 0.891$, $P < 0.001$). The small or nearly zero $\Delta\rho$ and ΔDO indicate that the water column was vertically well-mixed due to the two long-lasting and strong DFW periods during middle

July and middle August. However, the water column was restratified within 5 days after the relaxation of the DFW with the $\Delta\rho$ increased from nearly zero to >10 kg m^{-3}. Correspondingly, bottom DO increased from <2 mg L^{-1} to around 5 mg L^{-1} during the strong DFW but decreased during the UFW, URW, and DRW.

Another noticeable characteristic is that two hypoxia episodes (DO fell below the green dashed line) were observed at the mooring site from July 4 to July 10 and from August 4 to August 7, respectively, when the UFW prevailed. Hypoxia diminished or disappeared once the strong DFW began and the plume shifted westward toward WCTZ. With the corresponding variation of DO, they showed the importance of wind-induced change in stratification, mixing, and transport to DO variation in the southwest of HK. DO has a more significant correlation ($R^2 = 0.468$, $P < 0.001$) with the alongshore wind stress than with river discharge ($R^2 = 0.039$, $P = 0.171$) in the ECTZ, suggesting DO in this region is more sensitive to the wind forcing under these conditions.

The temporally variable DO qualitatively correlates with the wind, river discharge, and the associated stratification. However, the quantitative DO responses to the change in intensity of each of these forcings are not evident from the observations because the variations are forced simultaneously by time-dependent multistressors. Moreover, the bottom DO and hypoxia vary spatially in response to these stressors, which we will explore in Sections 3.2 and 4.

3.1.2. Spatial Variation of Hypoxia

The horizontal distribution of $\Delta\rho$, surface salinity, surface chlorophyll, and bottom DO in 2015 L1, 2017 L1, L2, and L3 were selected to show the spatial variability of eutrophication/hypoxia during the UFW, URW, DFW, and DRW, respectively (Figure 4).

During the UFW in 2015 (Figures 4a–4c), the salinity increased from <10 PSU inside the PRE to 24 PSU in the CTZ. The northeastward wind-driven currents advected the river plume eastward over the shelf after the freshwater discharged from the PRE and formed a strong stratification (large $\Delta\rho$) over the CTZ. Primary production peaked in the CTZ with sufficient light, nutrient, and residence time for the growth and accumulation of phytoplankton (Li et al., 2020). Thus, relatively low DO was observed at the bottom of the CTZ (Figure 4c), although hypoxia was relatively weak due to the low river discharge in 2015 (Figure 2a).

The relaxing UFW and URW and the abnormally large river discharge (Figure 2a) that occurred before and during the cruise of 2017 L1 led to an extensive surface plume and robust stratification over the adjacent southwestern shelf (Figure 4d) when the plume veered westward after freshwater discharged from the outlets along the west bank of the estuary (Figure 1). Correspondingly, the distribution of chlorophyll (Figure 4e) showed distinct bloom in the plume region with chlorophyll >10 μg L^{-1} stimulated by the abundant nutrient in the plume, as evidenced by the distribution of DIC and pH in Zhao et al. (2020). Similar high chlorophyll concentration (>30 μg L^{-1}) was observed in the middle CTZ in the summer of 2010 under suitable biophysical conditions (Lu & Gan, 2015). Hypoxia occurred within the 20 m isobath in the CTZ and was more severe than in 2015, mainly due to the abnormally large river discharge in 2017 (Figure 2a).

During the continuous DFW in 2017 L2 (Figures 4g–4i), the plume flowed along the west coast, forming a narrow front indicated by the dense nearshore isohalines. The stratification was weakened in the CTZ by the combined effects of DFW and dramatically decreasing river discharge (Figure 2a). The westward current shifted the surface high-chlorophyll water farther west. The bottom hypoxia disappeared in the ECTZ for the lack of surface primary production and weakened stratification. Hypoxia in the WCTZ was also weaker than that in 2017 L1 because the continuous strong DFW swiftly advected the nutrient-rich plume water westward.

During the DRW in 2017 L3, when the westward DFW weakened, the surface plume spread eastward (Figure 2a) and $\Delta\rho$ slightly increased relative to 2017 L2 in the CTZ. Surface chlorophyll was lower (<4 μg L^{-1}) in the WCTZ while was elevated in the ECTZ (>6 μg L^{-1}, Figure 4k). Nevertheless, hypoxia was enhanced in both WCTZ and ECTZ compared to 2017 L2.

In summary, the geographical locations and intensity of hypoxia vary with the external stressors (i.e., wind and river discharge) in the CTZ. Hypoxia variability somehow relates to surface eutrophication and stratification, which is ultimately regulated by the variability of wind-driven transport of the nutrient-rich river plume and associated biophysical condition. However, given the complexity of the estuarine-shelf system,

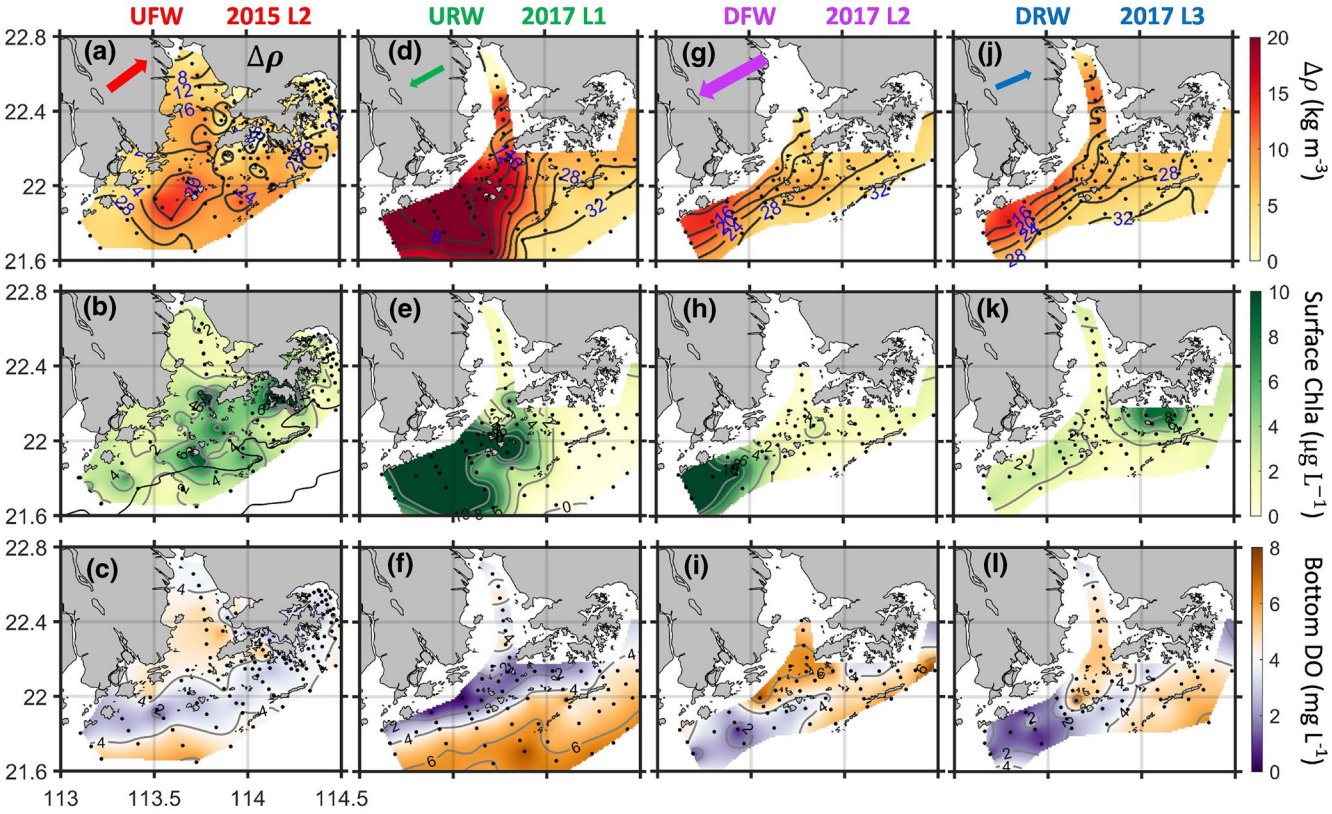

Figure 4. Horizontal distributions of (upper panel) bottom and surface density difference ($\Delta\rho$, kg m^{-3}, colored contours) and surface salinity (gray contours, with a contour interval of 4 PSU), surface chlorophyll (Surf. Chl., μg L^{-1}, middle), and bottom DO (Bot. DO, mg L^{-1}, lower panel) during cruises in 2015 and 2017 under different wind conditions indicated by the colored arrows with the size of arrows represent the intensity of alongshore wind stress averaged during the survey period. UFW: upwelling-favorable wind; URW: upwelling-favorable wind relaxation; DFW: downwelling favorable wind; DRW: downwelling favorable wind relaxation.

limited observations alone are not sufficient to quantitatively identify the hypoxia response to each forcing component of the varying external forcings and their nonlinear interactions. We thus used numerical simulations to extract the underlying processes and biophysical forcing mechanism of the observed variability of hypoxia.

3.2. Model Results

In this section, we follow the observed results and investigate the biophysical responses to the wind transition from UFW to URW, DFW, and DRW in the model results. The horizontal surface circulation, bottom detritus, bottom vertical mixing, and DO during UFW averaged from neap to spring tide (from Day 38 to Day 45) in the control run W1 and during DRW (Day 32), DFW (Day 45), and DRW (Day 50) in Case W2 are shown in Figure 5. Figure 6 shows the vertical distributions of biophysical factors and their differences between Cases W1 and W2 along Transect A during different wind transition periods. We calculate the nitrogen flux (i.e., the sum of nitrogen in the form of NO_3, NH_4, small detritus, large detritus, phytoplankton, and zooplankton, Figure 7) that crosses the four boundaries of the WCTZ and ECTZ forced by the steady UFW in Case W1 and varying wind in Case W2, respectively. Differences (W2 minus W1) in the nitrogen flux illustrate the response of nutrient transport to the unstable wind. The variation of HA of Cases W1 and W2 is shown in Figure 8.

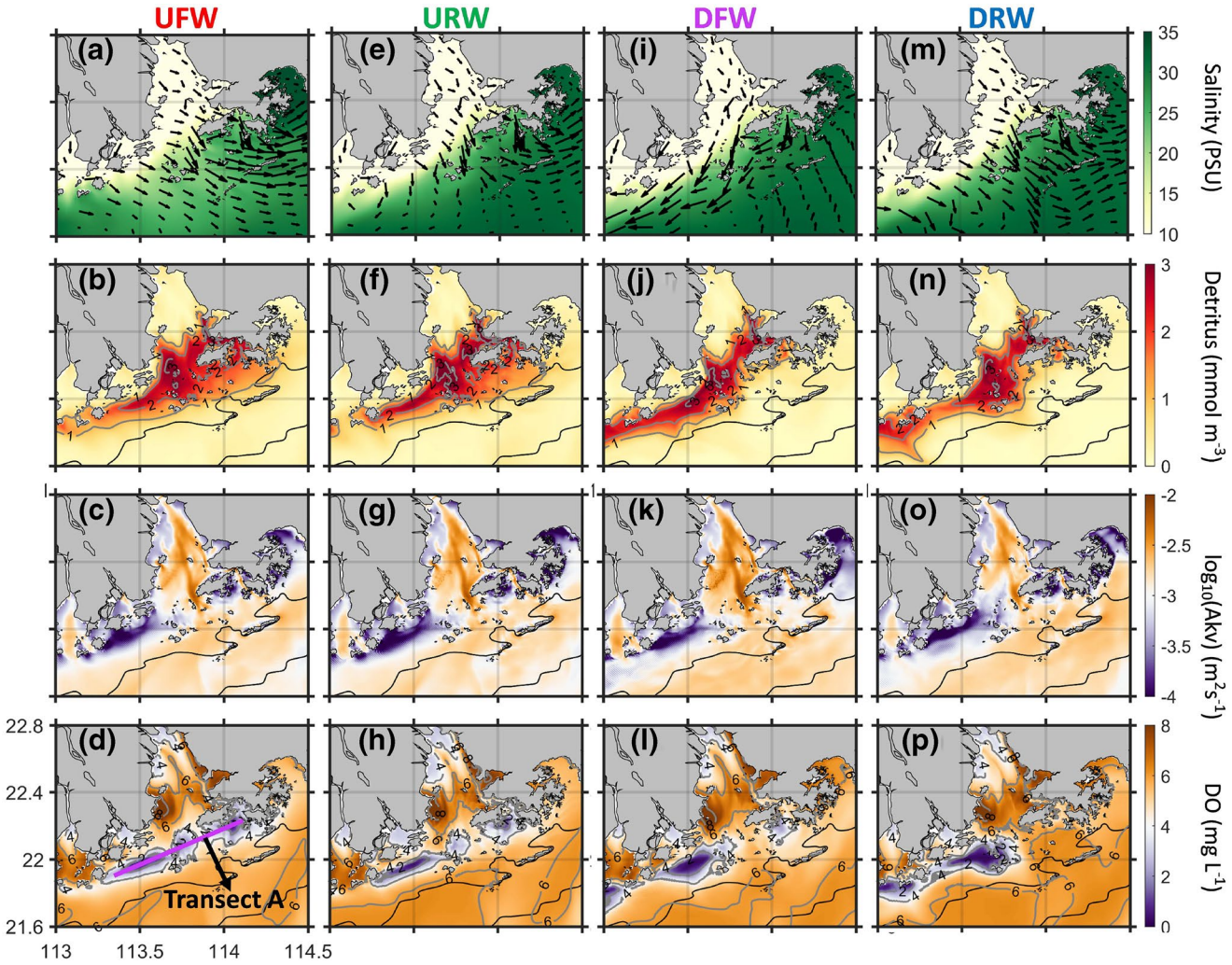

Figure 5. The horizontal distributions of surface salinity (Salt., color contours, first panel) and velocity (vectors, m s^{-1}), depth-averaged detritus within 2 m of the bottom (mmol N m^{-3}, second panel), the logarithm of depth-averaged vertical mixing coefficient within 2 m of the bottom (log_{10}(AKv), m^2 s^{-1}, third panel), and bottom DO (mg L^{-1}, bottom panel) during (a–d) UFW of Case W1 averaged from Day 38 to Day 45, (e–h) DRW (Day 32), (i–l) DFW (Day 45), and (m–p) DRW (Day 50) of Case W2. The magenta line in (d) shows the location of Transect A that we used in Figure 6.

3.2.1. Upwelling

During the UFW, the currents flow offshore and eastward at the surface and landward at the bottom of the CTZ and shelf. Freshwater discharge is spatially asymmetric with the lower salinity water veering along the west coast before it spreads eastward due to the effect of earth rotation (Figures 5a and 6a). Distribution of bottom detritus resulting from the mortality of planktons mostly resembles the distribution pattern of surface chlorophyll along the convergent zones in the CTZ where the concentration is >2 mmol m^{-3} (Figures 5b and 6b). The convergence is related to the vortex flow formed by the horizontal velocity shear between the wind-driven shelf current and the plume, which provides a favorable condition for the accumulation of organic matter and the hypoxia formation (Li et al., 2020).

In addition to the organic matter accumulation, the CTZ, especially the WCTZ, exhibits weaker bottom vertical mixing coefficient (AKv, $<10^{-4}$ m^2 s^{-1}, Figures 5c and 6c) due to the strong stratification caused by the surface plume water and dense bottom seawater, indicated by the strong halocline (Figure 6a). Consequently, the most severe bottom oxygen depletion occurs in the CTZ with the HA in the WCTZ about twice as large as in the ECTZ (Figures 5d and 8). The coherent pattern in biophysical variables and hypoxia is consistent with that observed in the cruise of 2015 (Figures 4a–4c).

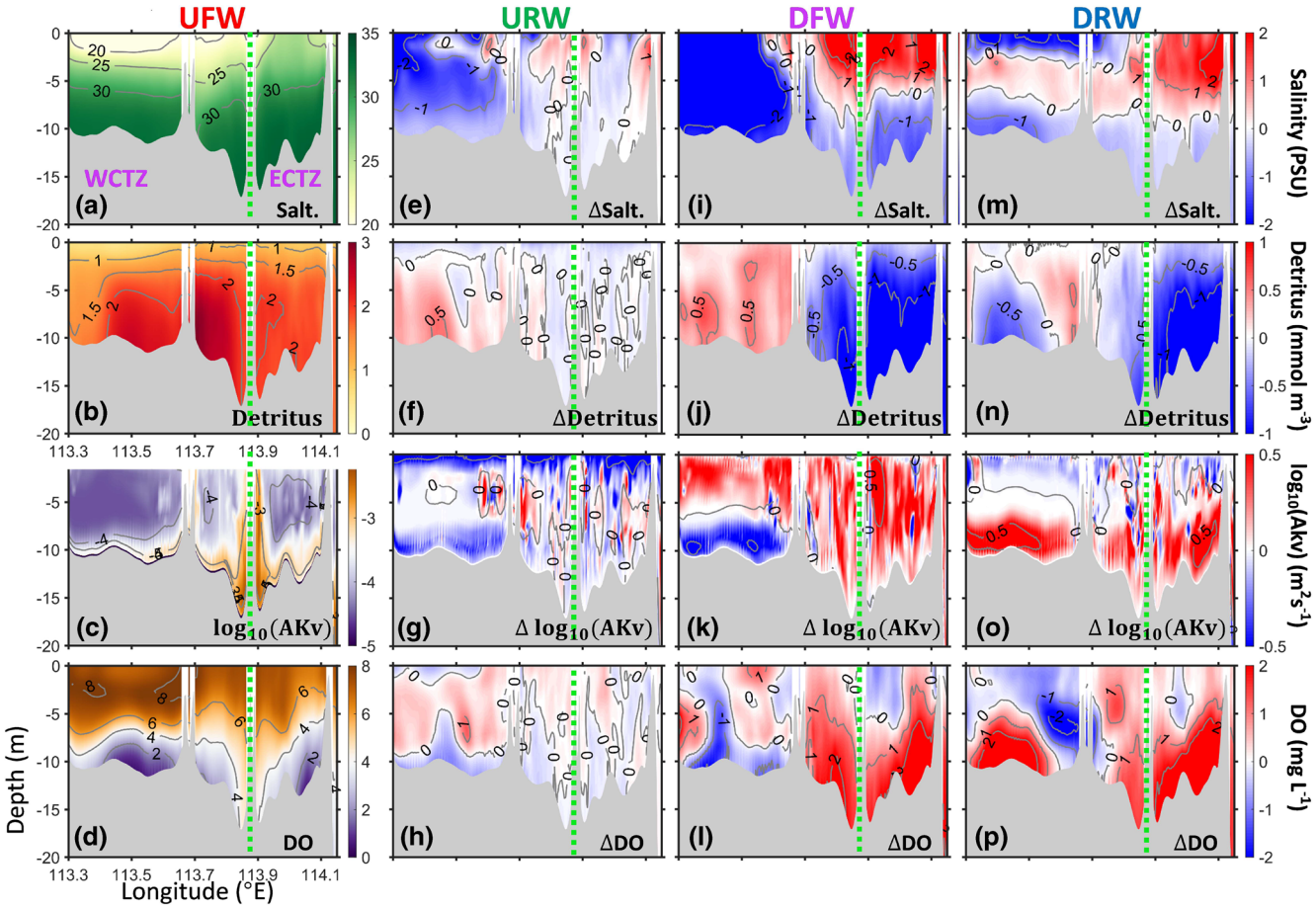

Figure 6. Vertical distributions of (a) salinity (Salt., PSU), (b) detritus (mmol N m^{-3}), (c) logarithm of vertical mixing coefficient (AKv, m^2 s^{-1}), (d) DO (mg L^{-1}) along Transect A (Figure 5d) during UFW of Case W1 averaged from Day 38 to Day 45. Vertical distributions of the differences in salinity (ΔSalt, PSU), detritus (ΔDetritus, mmol N m^{-3}), the logarithm of vertical mixing coefficient (ΔAKv, m^2 s^{-1}), and DO (ΔDO, mg L^{-1}) between Case W2 and Case W1 along Transect A during the (e)–(h) DRW (Day 32), (i–l) DFW (Day 45), and (m–p) DRW (Day 50). The green dashed lines separate the WCTZ and ECTZ. WCTZ, western coastal transition zones; ECTZ, eastern coastal transition zones.

Figures 7a and 7b show that the nitrogen fluxes in the CTZ reach a quasi-steady state and fluctuate with the tides during steady UFW. The results indicate that the WCTZ and ECTZ share similar characteristics: (1) nitrogen enters the two regions through the northern and western boundaries and exits through the southern and eastern borders; (2) the nitrogen fluxes across the southern and eastern boundaries are comparable; (3) the sum of the total nitrogen fluxes is positive, implying the utilization through biological processes. However, the flux through the western boundary contributes less to the WCTZ than to the ECTZ, which can be attributed to the eastward-flowing coastal current during UFW and the path of the nutrient sources discharged from the PRE.

3.2.2. Upwelling Relaxation

We now examine the effects of variable wind forcing on the biophysical processes by comparing Case W2 to Case W1. As UFW weakens during URW (Days 31–35, Figures 5e–5h and 6e–6h), the eastward coastal current weakens, or a westward current develops over the CTZ. River plume veers westward, and detritus increases in the WCTZ but decreases in the ECTZ. The change is also reflected in the nutrient transport (Figures 7c–7f). In the WCTZ, the most dramatic change is the nitrogen flux crossing the western boundary, which changes from positive (~0.12×10^6 mmol s^{-1}, influx) to negative (~-1.3×10^6 mmol s^{-1}, outflux). The opposite change (i.e., from negative to positive) occurs along the southern and eastern boundaries caused by the weakening UFW. Simultaneously, the southward nitrogen influx across the northern bound-

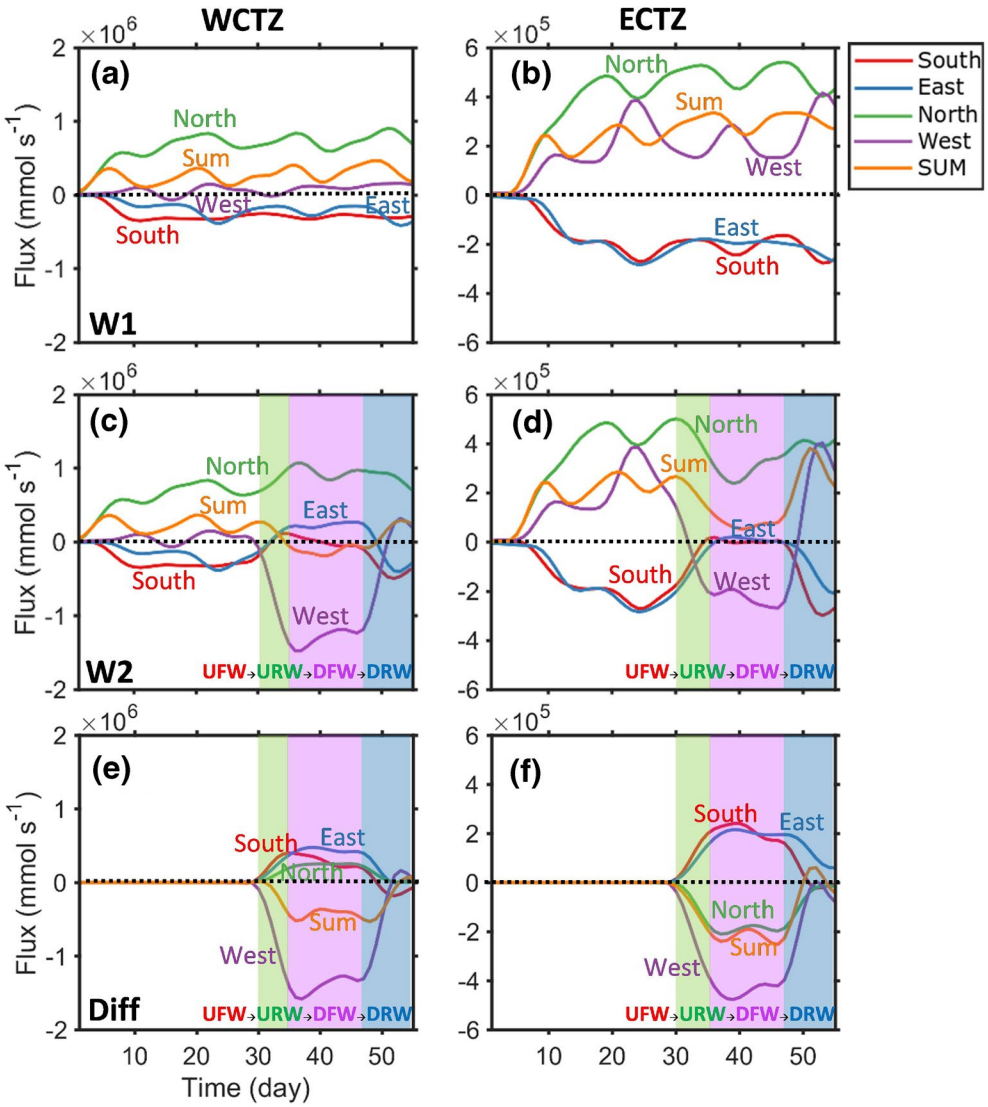

Figure 7. Time series of the depth-integrated nitrogen fluxes crossing different boundaries of the WCTZ (left) and ECTZ (right) in (a), (b) Case W1, in which upwelling wind persistently prevailed; (c), (d) Case W2, in which the wind varied from UFW (0.025 Pa, Days 1–30), URW (Days 31–35), DFW (−0.025 Pa, Days 36–47), and DRW (Days 48–55) shown by the colored shaded areas, and (e), (f) the difference between the two cases (W2 minus W1). Nitrogen flux is the sum of nitrogen in the form of NO_3, NH_4, small detritus, large detritus, phytoplankton, and zooplankton. South, East, North, and West represent the fluxes across the southern, eastern, northern, and western boundaries of the WCTZ and ECTZ defined in Figure 1b, respectively. SUM shows the net flux across the four boundaries of each zone with positive and negative value referring to the influx and outflux, respectively. WCTZ, western coastal transition zones; ECTZ, eastern coastal transition zones.

ary increases from ~0.66×10^6 to ~1×10^6 mmol s^{-1}. Similar changes occur along the western, southern, and eastern boundaries of the ECTZ, but the flux decreases across the northern boundary due to the westward-veering plume. Consequently, the net nitrogen flux (sum of four sections) decreases from ~0.27×10^6 to ~-0.1×10^6 mmol s^{-1} in the WCTZ and from ~2.7×10^5 to~1.3×10^5 mmol s^{-1} in the ECTZ during the URW, which would generally diminish the hypoxia.

However, the decreased net nitrogen flux during URW has little impact on the HA in the ECTZ but increases the HA in the WCTZ (blue lines in Figures 8a and 8b). The relatively significant change in nitrogen flux occurs in the WCTZ because the wind strongly affects the locally stratified plume water (Gan et al., 2009b), which generates more significant changes in the surface current and increases detritus by

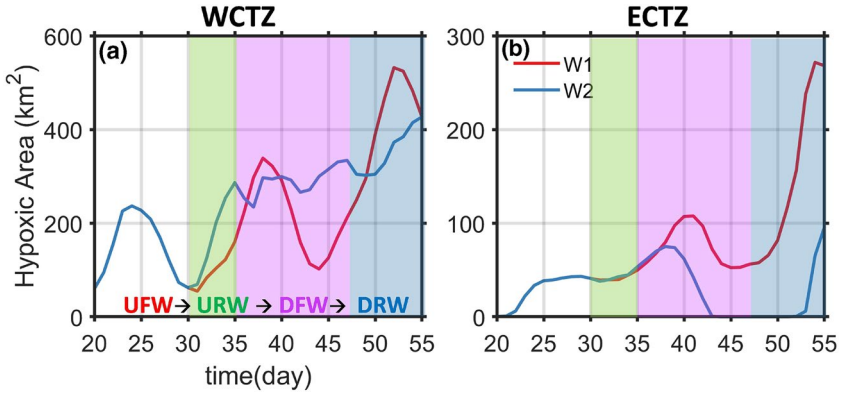

Figure 8. Comparisons of the responses of the hypoxia areas (HA, DO < 2 mg L^{-1}) for Case W1 (red lines) and W2 (blue lines) within the (a) WCTZ and (b) ECTZ. Shaded areas show the various stages of UFW, URW, DFW, and DRW for Case W2. WCTZ, western coastal transition zones; ECTZ, eastern coastal transition zones.

0.5 mmol N m^{-3} in the nearshore region of the WCTZ. Additionally, bottom vertical mixing weakens ($\Delta \log_{10}(AKv)$ ~−0.3 m^2 s^{-1}) due to the decreasing surface momentum input, and, thus, bottom DO decreases by 0.5 mg L^{-1} (Figures 6e–6h). In contrast, these effects offset each other in the ECTZ. The overall responses are related to the weakening UFW, seaward Ekman transport, and upwelling shelf circulation in the CTZ during URW. The simulation captured the observed variability pattern of the biogeochemical variables during the URW revealed in Section 3.2.

3.2.3. Downwelling

Fifteen days after the onset of the URW and the ensuing DFW, the eastward surface current during UFW reverses and the plume flows westward, which shrinks the freshwater into the narrow coastal waters with a deep halocline in the WCTZ but increases upper layer salinity in the ECTZ (Figures 5i and 6i). The negative ΔSalt at the bottom of the CTZ results from the onshore Ekman transport and downwelling of the plume waters. Under the control of the downwelling circulation from Day 35 to Day 47 in Case W2, the negative nitrogen flux flowing out from western boundaries is about ~5.6 times of the influx through the eastern border and ~1.3 times of the flux across the northern section, which lead to a negative net flux (~-1.2×10^5 mmol s^{-1}) in the WCTZ (Figure 7c). Meanwhile, in the ECTZ, the decreasing influx across the northern boundary still exceeds the increasing western outflux and leads to the decreasing positive net flux (~0.7×10^5 mmol s^{-1}, Figure 7d). A relatively small influx occurs along the southern and eastern boundaries in both the WCTZ and ECTZ, reflecting the minor effects of onshore nitrogen transport. Unsurprisingly, HA decreases in the ECTZ compared to its size during the steady UFW condition (Figure 8).

The detritus increases by >0.5 mmol m^{-3} in the western side of WCTZ along the convergent belt but decreases by over 1 mmol m^{-3} in the middle CTZ and ECTZ (Figures 5j and 6j). The vertical mixing increases in the entire CTZ (Figure 5k) except at the bottom of the WCTZ (Figure 6k), where the strong stratification suppresses the mixing. Under the combined effects of detritus and mixing, the bottom hypoxia extends and migrates westward in the WCTZ but disappears on Day 43 in the ECTZ in Case W2 (Figures 5l and 6l). These responses largely resemble the observed pattern in the 2017 L2 (Figures 4g–4i).

3.2.4. Downwelling Relaxation

When the DFW relaxes to UFW during the DRW (Days 48–50 in Case W2), the plume starts to expand offshore and eastward as the offshore Ekman drift strengthens. The net nitrogen fluxes increase and return to their states during the UFW (Figure 7), although the changes during DRW are asymmetric with those during the URW. The salinity is still lower in the WCTZ and higher in the ECTZ, but ΔSalt is decreased compared to that during the DFW (Figures 5m and 6m). The detritus reduces quickly in the WCTZ but gradually increases in the middle CTZ and the ECTZ (Figure 6n) when the westward spreading of the plume weakens during DRW, as shown by the changing ΔDetritus from DFW (Figure 6j) to DRW (Figure 6n). Similar results are also shown by the corresponding horizontal distributions in Figures 5j and 5n. Besides, bottom vertical

mixing reflected by vertical mixing coefficient, AKv, is enhanced markedly along the CTZ (Figures 5o and 6o) primarily due to the strengthening onshore current at the bottom and the vertical shear (not shown), although the surface AKv is still small due to the weaker wind-induced mixing during DRW. With a relatively lower detritus concentration and more vigorous bottom mixing, the bottom DO is 1 mg L^{-1} higher in the CTZ, leading to a smaller HA during the DRW relative to the UFW. HA slowly increases in the WCTZ, while hypoxia reoccurs in ECTZ after Day 52 during URW to UFW (Figure 8).

In summary, wind direction and intensity influence the general circulation, nutrient flux, bottom detritus distribution, vertical mixing intensity, and, consequently, the bottom DO. The strong stratification and sufficient detritus lead to two hypoxic centers in the convergence zones of the CTZ during the UFW. Compared to the steady UFW, westward onshore advected detritus and weakened mixing are favorable for the hypoxia development during the URW and DFW in the WCTZ. However, the effects of decreasing detritus and AKv on hypoxia offset each other during the URW. The hypoxia consequently disappears during DFW in the ECTZ under the combined impact of lacking detritus and enhanced mixing. Contrarily, DRW tends to restore the biophysical variables to their previous states during UFW and accounts for opposite changes in detritus in the WCTZ and ECTZ.

4. Discussion

4.1. Dislocation of Surface Eutrophication and Bottom Hypoxia

DO is closely related to surface eutrophication. Climatologically, it generally shows a good match between regions with high chlorophyll at the surface and low DO at the bottom (Li et al., 2020). However, dislocation of surface high-concentration of nutrient and chlorophyll and bottom hypoxia was found based on the cruise observation and in previous studies (Zhao et al., 2020), which have not been fully discussed. The time needed for the growth of phytoplankton, sinking, and remineralization processes, etc., and the lateral transport of nutrient and organic matter are the determining factors that account for the dislocation. A coastal current with a speed of 0.2 m s^{-1} can lead to a spatial disparity between the phytoplankton growth rate and biomass of 103 km and a 6-days time lag between nutrients and phytoplankton in the river plume (Gan et al., 2014). So the weak or lack of correlation between bottom DO and surface NO_3 from the cruises data ($P > 0.001$, Figure 2c) can be attributed to the swift changes in wind-driven circulation and the time lag between surface eutrophication and bottom oxygen depletion. However, mixing-induced changes in stratification and DO are almost simultaneous (Figures 2b and 3).

The spatial dislocation was also observed in the cruise observations. During the 2017 L1 (Figures 4d–4f), although the URW and extreme large river discharge changed the distribution of plume and primary production at the surface, the bottom current remained shoreward during URW due to the pumping of downstream outflow (Gan et al., 2015; Zu & Gan, 2015) and created a strong stratification that facilitated oxygen consumption and the development of hypoxia at the bottom. Hypoxia occurred within the 20 m isobath in the WCTZ in 2017 and was more severe than in 2015, mainly due to the abnormally large river discharge (Figure 2a). Nevertheless, the sinking and deposition of organic matter originated from the surface bloom during 2017 L1 continued to fuel the DO depletion and, with the simultaneously weakened wind-induced mixing, facilitated the hypoxia development in the WCTZ afterward. Consequently, hypoxia was enhanced in WCTZ compared to 2017 L1, with its pattern resembled the surface high chlorophyll about 10 days ago during 2017 L1.

The time lag between the surface phytoplankton bloom and bottom oxygen consumption and the swift changes in two-layer wind-driven estuarine circulation increase the complexity of the system and lead to the spatially and temporally inconsistent distribution of surface eutrophication and bottom hypoxia, especially in the observation. The simulation with steady forcings of river discharge and wind neglects the complexity of unsteady states in both biogeochemical and physical processes.

4.2. Quantifying the Variability of Hypoxia

The biophysical variation in Case W2 demonstrates the significant impact of wind transition on the changes in nutrient, detritus, AKv, and DO in the CTZ. The responses are also modulated by the simulta-

neous variation of discharges of freshwater (buoyancy), as shown in the observational results (Section 3). Effects of wind and river discharge on hypoxia are related to two processes in the CTZ: (1) the distribution of the river plume, associated nutrient, and detritus driven by the plume and the wind-driven coastal current; (2) the regulation on the water column stratification, vertical mixing, and residence time (RT) by wind and freshwater discharge. Specifically, Process (1) provides nutrient and organic matter as a necessary condition for eutrophication and determines the time scale of hypoxia occurrence. The combination of Process (1) with Process (2) forms a sufficient condition for the formation of eutrophication and hypoxia in the CTZ (Li et al., 2020). We observed these two processes controlling the hypoxia variability when hypoxia expanded during weak UFW, diminished by wind-induced vigorous mixing during the DFW, and reoccurred within several days during the UFW in both cruise data (Figure 2a) and buoy time series (Figure 3).

We investigated the quantitative responses of the biophysical factors to the varying wind magnitude and river discharge and their nonlinear impact on hypoxia variability. We conducted a set of experiments from Day 30 in Case W1 and applied constant forcing but different from Case W2 (i.e., wind, river discharge) from Day 31 onward. For convenience, we define the river index (RI) as the ratio of river discharge used in the sensitivity tests to typical river discharge (18,400 $m^3\ s^{-1}$) used in Case W1 and the wind index (WI) as the ratio of wind to the typical UFW (e.g., W-2R1.3 means the alongshore wind stress = −0.05 Pa and River discharge = 23,920 $m^3\ s^{-1}$). WI < 0 refers to the DFW and WI > 0 refers to UFW.

Figure 9 shows the key biophysical factors averaged from Day 38 to Day 45 (from neap to spring tide) within the bottom 2 m of the hypoxia centers in the WCTZ and ECTZ to illustrate the biophysical responses to the changing DFW intensity and river discharge based on the numerical experiments. The net oxygen consumption (NOC) is calculated based on the oxygen equation (Equation 1), which is the sum of photosynthesis, nitrification, metabolism, and remineralization in the water column and bottom sediment oxygen demanding. Furthermore, the residence time (RT) is defined by the time that water masses stay in a specific region. We used a parcel-tracking Euler technique to record the residence time of water masses in the PRE following Liu and Gan (2017). The residence time is over 10 days in the convergent zones of the PRE (Li et al., 2020), which provides sufficient time for deposition and remineralization of detritus that is generally characterized by about 6–10 days (Cui et al., 2019; Lu et al., 2018). Sufficient residence time is crucial to the development of hypoxia and the ratio of RT to the time of hypoxia occurrence ($T_{hyp} = \frac{\text{initial } O_2}{NOC}$) is usually used as the hypoxia generation index ($HGI = \frac{T_{hyp}}{RT}$). HGI < 1 is the necessary condition for hypoxia to form (Fennel & Testa, 2019).

The HGI, determined by initial DO, NOC, and RT, varies with the wind direction and magnitude and differs in the WCTZ and ECTZ. In the WCTZ, the smallest HGI (~0.2) occurs at the weaker wind forcing or current with the longest RT of 10 days (not shown here) at WI = 0 and contributes to the largest HA. HGI gradually increases asymmetrically with increasing wind intensity for UFW and DFW. There is a dramatic increase in HGI at WI = −2 when RT decreases sharply by 2 days and detritus or NOC slightly drops when the strong wind-driven coastal current sweeps waters westward. However, HGI decreases with increasing WI in the ECTZ because more organic matter is advected eastward when the wind changes from DFW to UFW. HGI is <1 except at WI = −2 and RI = 0.5 in the ECTZ and is much larger in the ECTZ, which is the main reason for the lack of or neglectable hypoxia in the ECTZ under those conditions.

Although HGI is useful to determine whether a system is favorable for hypoxia formation, it cannot fully explain the hypoxia variability in the WCTZ for different scenarios with HG1 < 1. Oxygen diffusion through wind-induced mixing can erode the hypoxic layer and reduce HA, as found in Changjiang Estuary (Zhang et al., 2019). AKv in the WCTZ is much smaller than in the ECTZ, which also contributes to the larger HA in the WCTZ (Figure 9). Bottom vertical mixing reaches a maximum at WI = −2 when RI remains unchanged and is responsible for the dramatic decrease in HA in the entire CTZ, also in the WCTZ where HGI is <1. Bottom AKv is asymmetric with a smaller value under DFW than that under the same magnitude UFW (e.g., WI = 1 and −1) in the CTZ because the DFW weakens the prevailing upwelling circulation in the entire water column before it eventually forms westward currents at the surface (Figure 5i) (Liu et al., 2018).

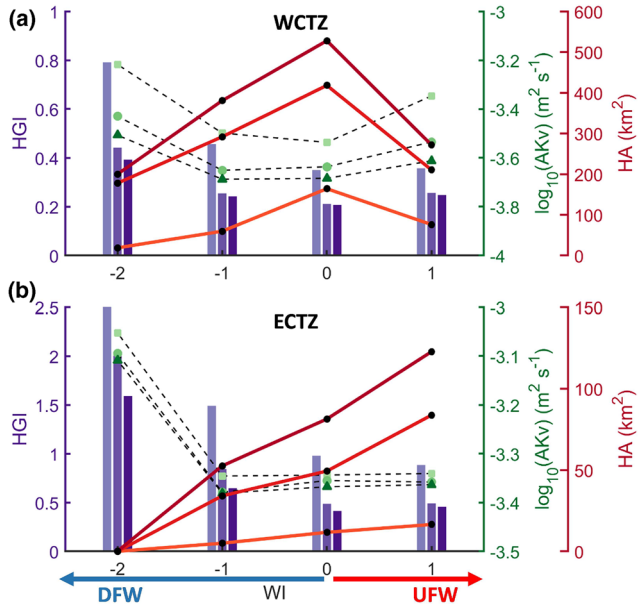

Figure 9. Hypoxia generation index (HGI, purple bars), vertical mixing coefficient (AKv, $m^2\ s^{-1}$, green dashed lines with triangles) and bottom hypoxic area (HA, km^2, red lines with black dots) in response to varying wind index (WI) and river index (RI) averaged in the 2 m above the bottom within the hypoxic centers in the (a) WCTZ and (b) ECTZ averaged from neap to spring tide (Day 38 to Day 45) during DFW from numerical experiments. Here, RI is the ratio of river discharge used in the sensitivity tests to standard river discharge (18,400 $m^3\ s^{-1}$) and WI is the ratio of wind to typical UFW (23° anticlockwise to the true east, 0.025 Pa). Thus, WI < 0 refers to the DFW and WI > 0 refers to UFW. The red and blue arrows under the bottom axis direct toward the strengthening UFW and DFW, respectively. The light to dark colors in each group show RI equal to 0.5, 1, and 1.3, respectively. WCTZ, western coastal transition zones; ECTZ, eastern coastal transition zones.

River discharge, as the source of buoyancy flux and nutrient flux, plays an essential role in hypoxia variability. Both HGI and AKv change monotonically with increasing river discharge, which contributes to the increasing HA in the CTZ. However, variations in HGI, AKv, and HA nonlinearly relate to the RI in different regions. Take the biophysical responses in the WCTZ at WI = 1 as an example, HGI decreases from 0.79 to 0.44, then to 0.39 when RI increases from 0.5 to 1.3, with $\log_{10}$ (AKv) reduction from −3.2 to −3.4, and finally to −3.5. Correspondingly, HA decreases by 61% compared to RI = 1 and increases by 29% from RI = 1 to RI = 1.3, suggesting the slower biophysical responses at higher river discharge. Thus, increased RI has a relatively smaller effect on hypoxia because the water column is generally stable enough, and surface eutrophication and bottom oxygen consumption quickly saturate with the increasing river discharge. At the same time, increasing RI decreases the residence time, which weakens the effect of eutrophication. On the other hand, the impact of increasing RI on hypoxia is also determined by the WI, e.g., HGI > 1 and HA = 0 at WI = −2 for all RI in the ECTZ.

In short, the effects of wind and river discharge on HA variation can be quantified by the ratio of the time scale for hypoxia occurrence and residence time (i.e., HGI) and vertical mixing (AKv). Figure 10 summarizes the responses and dynamics of hypoxia variability under different wind and river forcings. HA emerges when HGI < 1 and tends to increase with decreasing HGI and AKv. Smaller HGI and AKv generally occur at weak wind forcing, and consequently, account for larger HA. Compared to steady UFW, DFW is favorable for hypoxia development when DFW < 0.05 Pa but can destroy hypoxia when DFW > 0.05 Pa in the WCTZ. It is unfavorable for hypoxia in the ECTZ due to the dramatic decrease in detritus and the associated increase in HGI for the west-veering plume. This suggests that the prolonged duration of DFW reported in the Gulf of Mexico, e.g., totally destroyed the preexisting upwelling dynamics background, may not frequently occur in the coastal ocean under the intermittent URW and ensuing DFW in the UFW prevailing season, such as in the Oregon coast (Gan & Allen, 2002) and the CTZ off the PRE in this study. The HA expanding rate reduces at a higher river discharge in the CTZ for the decreasing residence time once the surface eutrophication and bottom oxygen consumption are saturated. This quantification method presented in our study combines the nonlinear effect of wind direction, wind intensity, and river discharge, which is more practicable in the PRE and other shallow estuarine systems with variable hypoxia forced by intermittent UFW, URW, DFW, and DRW during a synoptic cycle. Besides, this is a more comprehensive assessment of hypoxia variability in response to the varying wind and river discharge compared to analysis based on statistical wind direction and duration that may ignore the detailed transient response during the prevailing UFW season.

5. Conclusions

Spatiotemporal development and dissipation of eutrophication/hypoxia in the CTZ between the Pearl River Estuary and the adjacent continental shelf off Hong Kong in response to varying external stressors (i.e., wind and river discharge) was investigated based on the field observations and a coupled physical-biogeochemical numerical model.

Repeated field observations show that bottom DO and hypoxia correlates highly with the wind and river discharge. The cruise measurements and numerical simulations reveal the spatially dependent biophysical responses during the wind transitions from UFW, URW, DFW, and DRW. We saw that wind direction and intensity influence the general circulation, nutrient flux, bottom detritus distribution, vertical mix-

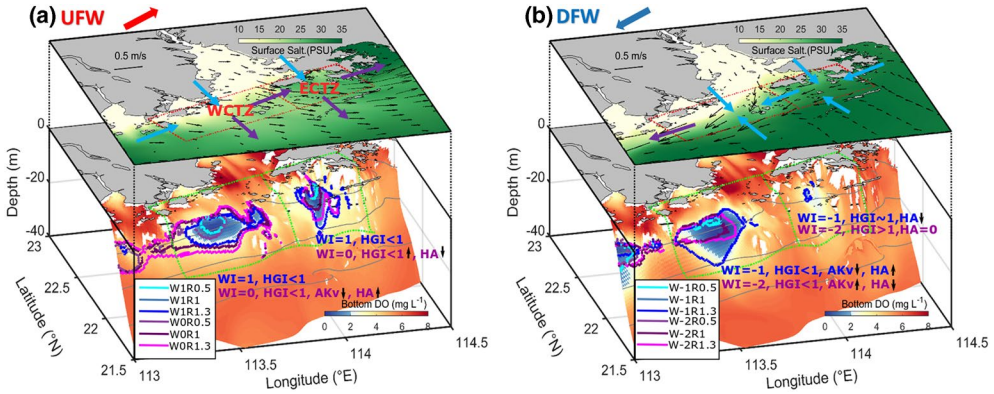

Figure 10. Conceptual sketch for the dynamics of hypoxia variability under different wind forcings. (a) and (b) show the surface salinity and bottom DO averaged from Day 38 to Day 45 in Case W1 and Case W2, respectively. The HA changes with varying wind index (WI) and river index (RI) are shown by different colored lines. The red and green dashed squares show the location of WCTZ and ECTZ at the surface and bottom, respectively. The blue and purple arrows show the respective influx and outflux of nitrogen across the boundaries of WCTZ and ECTZ.

ing, and consequently, bottom DO and hypoxia in the CTZ. The convergence zones provide a favorable condition for the accumulation of detritus and the formations of two hypoxia centers in the WCTZ and ECTZ under the UFW, respectively. Compared with the steady UFW, the westward and onshore transport of detritus and the weakened mixing are favorable for the hypoxia development during the URW and DFW in the WCTZ. However, the effects of decreasing detritus and mixing offset each other during the URW, and hypoxia disappears under the combined effects of lacking detritus and enhanced mixing during DFW in the ECTZ. Contrarily, DRW tends to restore the biophysical variables to their previous states during the UFW.

We found the spatially variable and nonlinear interactions between varying wind-driven shelf circulation and river discharge, which regulate the transport of nutrient, distribution of detritus, mixing and residence time, and thus, the high variability of hypoxia over the CTZ (Figure 10). Combining all these factors, we use HGI and bottom mixing (AKv) to quantify the hypoxia variability under variable wind forcings and river discharge. The bottom mixing modifies HA based on the necessary conditions for hypoxia development of HGI < 1. Weak wind forcing corresponds to smaller HGI and AKv, and, consequently, larger HA. Spatially, DFW is favorable for hypoxia development in the WCTZ until further strengthening wind destroys the stratification. Conditions under DFW forcing are unfavorable for hypoxia formation in the ECTZ mainly due to decreased detritus concentration or net oxygen consumption due to the westward-veering current. The HA expansion rate reduces at a higher river discharge in the CTZ due to decreased residence time and enhanced stratification in the water column once the surface eutrophication and bottom oxygen consumption become saturated.

The complex changing patterns of environmental stressors of wind, river discharge, nutrient loading, etc., and their potential interactions make eutrophication and hypoxia highly variable in space and in time in the CTZ, as well as in other systems of the world's coastal oceans. The method considering the nonlinear effect of those stressors to quantify the hypoxia variability can also be applied to other shallow estuarine systems with variable hypoxia.

Appendix A: Biological Parameters

The biological parameters adopted in the NPPZD-oxygen model in the PRE were set based on previous studies in this region as shown in Table A1.

Table A1
Biogeochemical Model Parameters

Description	Value	Unit
Phytoplankton growth rate at 0 °C	0.59	day^{-1}
Light attenuation due to seawater	0.04	m^{-1}
Light attenuation by chlorophyll	0.025	m^{-1}
Initial slope of the P-I curve	0.125	mg C/(mg Chl W m^{-2} day)
Half saturation for phytoplankton NO_3 uptake	1.25	1/(mmol N m^{-3})
Half saturation for phytoplankton NH_4 uptake	1.25	1/(mmol N m^{-3})
Phytoplankton mortality rate	0.15	day^{-1}
Zooplankton maximum grazing rate	0.5	day^{-1}
Zooplankton assimilation efficiency for nitrogen	0.75	day^{-1}
Zooplankton basal metabolism	0.1	day^{-1}
Zooplankton specific excretion rate	0.1	day^{-1}
Zooplankton mortality rate	0.025	day^{-1}
Small detritus remineralization rate for nitrogen	0.3	day^{-1}
Large detritus remineralization rate for nitrogen	0.1	day^{-1}
Small detritus remineralization rate for phosphorus	0.3	day^{-1}
Large detritus remineralization rate for phosphorus	0.1	day^{-1}
Coagulation rate	0.1	day^{-1}
Sinking velocity for small detritus	1	m day^{-1}
Sinking velocity for large detritus	20	m day^{-1}
Sinking velocity for phytoplankton	1	m day^{-1}
Maximum nitrification rate	0.2	day^{-1}

Data Availability Statement

The model data for this study were produced by the community model ROMS (https://www.myroms.org/). The results used in the study are on the web site (https://ocean.ust.hk/data/?page_id=619).

Acknowledgments
This work was supported by the Theme-based Research Scheme (T21-602/16-R, OCEAN_HK project) of the Hong Kong Research Grants Council. The authors thank all members who participated in the cruises organized by OCEAN_HK. Center for Ocean Research in Hong Kong and Macau is a joint ocean research center between National Laboratory for Marine Science and Technology (QNLM) and Hong Kong University of Science and Technology (HKUST). The authors are grateful to the National Supercomputer Center of Tianhe-1 (Tianjin) and Tianhe-2 (Guangzhou).

References

Adams, K. A., Barth, J. A., & Chan, F. (2013). Temporal variability of near-bottom dissolved oxygen during. *Upwelling off Central Oregon*, *118*(10), 4839–4854.

Breitburg, D., Levin, L. A., Oschlies, A., Grégoire, M., Chavez, F. P., Conley, D. J., et al. (2018). Declining oxygen in the global ocean and coastal waters. *Science*, *359*(6371), eaam7240. https://doi.org/10.1126/science.aam7240

Cai, W.-J., Dai, M., Wang, Y., Zhai, W., Huang, T., Chen, S., et al. (2004). The biogeochemistry of inorganic carbon and nutrients in the Pearl River estuary and the adjacent Northern South China Sea. *Continental Shelf Research*, *24*(12), 1301–1319. https://doi.org/10.1016/j.csr.2004.04.005

Carstensen, J., Andersen, J. H., Gustafsson, B. G., & Conley, D. J. (2014). Deoxygenation of the Baltic Sea during the last century. *Proceedings of the National Academy of Sciences of the United States of America*, *111*(15), 5628–5633.

Cui, Y., Wu, J., Ren, J., & Xu, J. (2019). Physical dynamics structures and oxygen budget of summer hypoxia in the Pearl River Estuary. *Limnology and Oceanography*, *64*(1), 131–148.

Diaz, R. J., & Rosenberg, R. (2008). Spreading dead zones and consequences for marine ecosystems. *Science*, *321*(5891), 926–929.

Egbert, G. D., & Erofeeva, S. Y. (2002). Efficient inverse modeling of barotropic ocean tides. *Journal of Atmospheric and Oceanic Technology*, *19*(2), 183–204.

Feng, Y., Fennel, K., Jackson, G. A., DiMarco, S. F., & Hetland, R. D. (2014). A model study of the response of hypoxia to upwelling-favorable wind on the northern Gulf of Mexico shelf. *Journal of Marine Systems*, *131*, 63–73.

Fennel, K., & Testa, J. M. (2019). Biogeochemical controls on coastal hypoxia. *Annual Review of Marine Science*, *11*, 105–130. https://doi.org/10.1146/annurev-marine-010318-095138

Fennel, K., Wilkin, J., Levin, J., Moisan, J., O'Reilly, J., & Haidvogel, D. (2006). Nitrogen cycling in the Middle Atlantic Bight: Results from a three-dimensional model and implications for the North Atlantic nitrogen budget. *Global Biogeochemical Cycles*, *20*, GB3007. https://doi.org/10.1029/2005gb002456

Gan, J., & Allen, J. S. (2002). A modeling study of shelf circulation off northern California in the region of the coastal ocean dynamics experiment: Response to relaxation of upwelling winds. *Journal of Geophysical Research*, *107*(C9), 3123. https://doi.org/10.1029/2000JC000768

Gan, J., & Allen, J. S. (2005). On open boundary conditions for a limited-area coastal model off Oregon. Part 1: Response to idealized wind forcing. *Ocean Modelling*, *8*(1–2), 115–133. https://doi.org/10.1016/j.ocemod.2003.12.006

Gan, J., Cheung, A., Guo, X., & Li, L. (2009a). Intensified upwelling over a widened shelf in the northeastern South China Sea. *Journal of Geophysical Research*, *114*, C09019. https://doi.org/10.1029/2007jc004660

Gan, J., Li, L., Wang, D., & Guo, X. (2009b). Interaction of a river plume with coastal upwelling in the northeastern South China Sea. *Continental Shelf Research*, *29*(4), 728–740. https://doi.org/10.1016/j.csr.2008.12.002

Gan, J., Lu, Z., Cheung, A., Dai, M., Liang, L., Harrison, P. J., & Zhao, X. (2014). Assessing ecosystem response to phosphorus and nitrogen limitation in the Pearl River plume using the Regional Ocean Modeling System (ROMS). *Journal of Geophysical Research: Oceans*, *119*, 8858–8877. https://doi.org/10.1002/2014JC009951

Gan, J., Wang, J., Liang, L., Li, L., & Guo, X. (2015). A modeling study of the formation, maintenance, and relaxation of upwelling circulation on the Northeastern South China Sea shelf. *Deep Sea Research Part II: Topical Studies in Oceanography*, *117*, 41–52.

Han, A., Dai, M., Kao, S.-J., Gan, J., Li, Q., Wang, L., et al. (2012). Nutrient dynamics and biological consumption in a large continental shelf system under the influence of both a river plume and coastal upwelling. *Limnology and Oceanography*, *57*(2), 486–502.

Harrison, P. J., Yin, K., Lee, J. H. W., Gan, J., & Liu, H. (2008). Physical–biological coupling in the Pearl River Estuary. *Continental Shelf Research*, *28*(12), 1405–1415. https://doi.org/10.1016/j.csr.2007.02.011

Hetland, R. D., & DiMarco, S. F. (2008). How does the character of oxygen demand control the structure of hypoxia on the Texas–Louisiana continental shelf? *Journal of Marine Systems*, *70*(1–2), 49–62.

Li, D., Gan, J., Hui, R., Liu, Z., Yu, L., Lu, Z., & Dai, M. (2020). Vortex and biogeochemical dynamics for the hypoxia formation within the coastal transition zone off the Pearl River Estuary. *Journal of Geophysical Research: Oceans*. *125*, e2020JC016178. https://doi.org/10.1029/2020JC016178

Liu, Z., & Gan, J. (2016). Open boundary conditions for tidally and subtidally forced circulation in a limited-area coastal model using the Regional Ocean Modeling System (ROMS). *Journal of Geophysical Research: Oceans*, *121*, 6184–6203. https://doi.org/10.1002/2016JC011975

Liu, Z., & Gan, J. (2017). Three-dimensional pathways of water masses in the South China Sea: A modeling study. *Journal of Geophysical Research: Oceans*, *122*, 6039–6054. https://doi.org/10.1002/2016JC012511

Liu, Z., & Gan, J. (2020). A modeling study of estuarine-shelf circulation using a composite tidal and subtidal open boundary condition. *Ocean Modelling*, *147*,101563. https://doi.org/10.1016/j.ocemod.2019.101563

Liu, Z., Gan, J., & Wu, X. (2018). Coupled summer circulation and dynamics between a bay and the adjacent shelf around Hong Kong: Observational and modeling Studies. *Journal of Geophysical Research: Oceans*, *123*, 6463–6480. https://doi.org/10.1029/2018JC013830

Lu, Z., & Gan, J. (2015). Controls of seasonal variability of phytoplankton blooms in the Pearl River Estuary. *Deep Sea Research Part II: Topical Studies in Oceanography*, *117*, 86–96.

Lu, Z., Gan, J., Dai, M., Liu, H., & Zhao, X. (2018). Joint effects of extrinsic biophysical fluxes and intrinsic hydrodynamics on the formation of hypoxia west off the Pearl River Estuary. *Journal of Geophysical Research: Oceans*, *123*, 6241–6259. https://doi.org/10.1029/2018jc014199

Mellor, G. L., & Yamada, T. (1982). Development of a turbulence closure model for geophysical fluid problems. *Reviews of Geophysics*, *20*(4), 851–875.

Ou, S., Zhang, H., & Wang, D.-x. (2009). Dynamics of the buoyant plume off the Pearl River Estuary in summer. *Environmental Fluid Mechanics*, *9*(5), 471–492. https://doi.org/10.1007/s10652-009-9146-3

Parsons, T. R. (2013). *A manual of chemical & biological methods for seawater analysis.*, Oxford: Elsevier.

Qian, W., Gan, J., Liu, J., He, B., Lu, Z., Guo, X., et al. (2018). Current status of emerging hypoxia in a eutrophic estuary: The lower reach of the Pearl River Estuary, China. *Estuarine, Coastal and Shelf Science*, *205*, 58–67. https://doi.org/10.1016/j.ecss.2018.03.004

Shchepetkin, A. F., & McWilliams, J. C. (2005). The regional oceanic modeling system (ROMS): A split-explicit, free-surface, topography-following-coordinate oceanic model. *Ocean modelling*, *9*(4), 347–404.

Siedlecki, S. A., Banas, N. S., Davis, K. A., Giddings, S., Hickey, B. M., MacCready, P., et al. (2015). Seasonal and interannual oxygen variability on the Washington and Oregon continental shelves. *Journal of Geophysical Research: Oceans*, *120*, 608–633. https://doi.org/10.1002/2014jc010254

Smolarkiewicz, P. K., & Margolin, L. G. (1998). MPDATA: A finite-difference solver for geophysical flows. *Journal of Computational Physics*, *140*(2), 459–480.

Spitz, Y. H., Allen, J. S., & Gan, J. (2005). Modeling of ecosystem processes on the Oregon shelf during the 2001 summer upwelling, *Journal of Geophysical Research*, *110*, C10S17. https://doi.org/10.1029/2005JC002870

Su, J., Dai, M., He, B., Wang, L., Gan, J., Guo, X., et al. (2017). Tracing the origin of the oxygen-consuming organic matter in the hypoxic zone in a large eutrophic estuary: The lower reach of the Pearl River Estuary, China. *Biogeosciences*, *14*(18), 4085–4099. https://doi.org/10.5194/bg-14-4085-2017

Wang, B., Hu, J., Li, S., & Liu, D. (2017). A numerical analysis of biogeochemical controls with physical modulation on hypoxia during summer in the Pearl River estuary. *Biogeosciences*, *14*(12), 2979–2999. https://doi.org/10.5194/bg-14-2979-2017

Wei, X., Zhan, H., Ni, P., & Cai, S. (2016). A model study of the effects of river discharges and winds on hypoxia in summer in the Pearl River Estuary. *Marine Pollution Bulletin*, *113*(1–2), 414–427. https://doi.org/10.1016/j.marpolbul.2016.10.042

Yin, K., Zhang, J., Qian, P.-Y., Jian, W., Huang, L., Chen, J., & Wu, M. C. S. (2004). Effect of wind events on phytoplankton blooms in the Pearl River Estuary during summer. *Continental Shelf Research*, *24*(16), 1909–1923. https://doi.org/10.1016/j.csr.2004.06.015

Yu, L., Gan, J., Dai, M., Hui, C. R., Lu, Z., & Li, D. (2020). Modeling the role of riverine organic matter in hypoxia formation within the coastal transition zone off the Pearl River Estuary. *Limnology and Oceanography*, https://doi.org/10.1002/lno.11616

Zhang, H., & Li, S. (2010). Effects of physical and biochemical processes on the dissolved oxygen budget for the Pearl River Estuary during summer. *Journal of Marine Systems*, *79*(1–2), 65–88. https://doi.org/10.1016/j.jmarsys.2009.07.002

Zhang, L., Yin, K., Wang, L., Chen, F., Zhang, D., & Yang, Y. (2009). The sources and accumulation rate of sedimentary organic matter in the Pearl River Estuary and adjacent coastal area, Southern China. *Estuarine, Coastal and Shelf Science*, *85*(2), 190–196. https://doi.org/10.1016/j.ecss.2009.07.035

Zhang, W., Wu, H., Hetland, R. D., & Zhu, Z. (2019). On mechanisms controlling the seasonal hypoxia hot spots off the Changjiang River estuary. *Journal of Geophysical Research: Oceans*, *124*, 8683–8700. https://doi.org/10.1029/2019JC015322

Zhang, W., Wu, H., & Zhu, Z. (2018). Transient hypoxia extent off Changjiang River estuary due to mobile Changjiang River plume. *Journal of Geophysical Research: Oceans*, *123*, 9196–9211. https://doi.org/10.1029/2018JC014596

Zhao, Y., Liu, J., Uthaipan, K., Song, X., Xu, Y., He, B., et al. (2020). Dynamics of inorganic carbon and pH in a large subtropical continental shelf system: Interaction between eutrophication, hypoxia, and ocean acidification. *Limnology and Oceanography*, *65*(6), 1359–1379. https://doi.org/10.1002/lno.11393

Zu, T., & Gan, J. (2015). A numerical study of coupled estuary–shelf circulation around the Pearl River Estuary during summer: Responses to variable winds, tides and river discharge. *Deep Sea Research Part II: Topical Studies in Oceanography*, *117*, 53–64. https://doi.org/10.1016/j.dsr2.2013.12.010

Zu, T., Wang, D., Gan, J., & Guan, W. (2014). On the role of wind and tide in generating variability of Pearl River plume during summer in a coupled wide estuary and shelf system. *Journal of Marine Systems*, *136*, 65–79.